



# A Study of Two Diffuse Dwarf Galaxies in the Field

Johnny P. Greco<sup>1</sup> , Andy D. Goulding<sup>1</sup>, Jenny E. Greene<sup>1</sup>, Michael A. Strauss<sup>1</sup> , Song Huang<sup>2</sup> ,  
Ji Hoon Kim<sup>3</sup> , and Yutaka Komiyama<sup>4,5</sup>

<sup>1</sup> Department of Astrophysical Sciences, Princeton University, Princeton, NJ 08544, USA; [jgreco@astro.princeton.edu](mailto:jgreco@astro.princeton.edu)

<sup>2</sup> Department of Astronomy and Astrophysics, University of California, Santa Cruz, 1156 High St., Santa Cruz, CA 95064, USA

<sup>3</sup> Subaru Telescope, National Astronomical Observatory of Japan, 650 N. Aohoku Pl., Hilo, HI 96720, USA

<sup>4</sup> National Astronomical Observatory of Japan, 2-21-1 Osawa, Mitaka, Tokyo 181-8588, Japan

<sup>5</sup> Department of Astronomy, School of Science, Graduate University for Advanced Studies (SOKENDAI), 2-21-1, Osawa, Mitaka, Tokyo 181-8588, Japan

Received 2018 April 10; revised 2018 August 31; accepted 2018 September 10; published 2018 October 17

## Abstract

We present optical long-slit spectroscopy and far-ultraviolet to mid-infrared spectral energy distribution fitting of two diffuse dwarf galaxies, LSBG-285 and LSBG-750, which were recently discovered by the Hyper Suprime-Cam Subaru Strategic Program (HSC-SSP). We measure redshifts using H $\alpha$  line emission and find that these galaxies are at comoving distances of  $\approx 25$  and  $\approx 41$  Mpc, respectively, after correcting for the local velocity field. They have effective radii of  $r_{\text{eff}} = 1.2$  and  $1.8$  kpc and stellar masses of  $M_{\star} \approx (2-3) \times 10^7 M_{\odot}$ . There are no massive galaxies ( $M_{\star} > 10^{10} M_{\odot}$ ) within a comoving separation of at least 1.5 Mpc from LSBG-285 and 2 Mpc from LSBG-750. These sources are similar in size and surface brightness to ultradiffuse galaxies, except they are isolated, star-forming objects that were optically selected in an environmentally blind survey. Both galaxies likely have low stellar metallicities  $[Z_{\star}/Z_{\odot}] < -1.0$  and are consistent with the stellar mass–metallicity relation for dwarf galaxies. We set an upper limit on LSBG-750’s rotational velocity of  $\sim 50 \text{ km s}^{-1}$ , which is comparable to dwarf galaxies of similar stellar mass with estimated halo masses  $< 10^{11} M_{\odot}$ . We find tentative evidence that the gas-phase metallicities in both of these diffuse systems are high for their stellar mass, though a statistically complete, optically selected galaxy sample at very low surface brightness will be necessary to place these results into context with the higher surface brightness galaxy population.

**Key words:** galaxies: dwarf – galaxies: general

## 1. Introduction

Low surface brightness (LSB) dwarf ( $M_{\star} \lesssim 10^9 M_{\odot}$ ) galaxies offer unique testing grounds for theories of galaxy formation and evolution. The relatively shallow gravitational potential wells of these systems make them highly sensitive to stellar feedback processes (e.g., Larson 1974; Dekel & Silk 1986; Governato et al. 2010; El-Badry et al. 2016), and as dark-matter-dominated systems, their ultralow stellar densities allow their dark matter distributions to be studied with little ambiguity from the challenges of quantifying the baryon component (e.g., de Blok et al. 2001; Marchesini et al. 2002). Moreover, their number densities and distribution of physical properties provide some of the most stringent tests of the dark energy plus cold dark matter ( $\Lambda$ CDM) paradigm (e.g., Weinberg et al. 2015; Bullock & Boylan-Kolchin 2017). Yet, our census of this important population, particularly beyond the Local Group, remains highly incomplete because optical surveys generally suffer from strong surface brightness selection effects (e.g., Disney 1976; Blanton et al. 2005).

The severity of this problem was recently underscored by the discovery of an abundant population of physically large, ultra-LSB galaxies in the Coma Cluster (ultradiffuse galaxies or UDGs; Koda et al. 2015; van Dokkum et al. 2015). These diffuse galaxies are characterized by red colors, smooth ellipsoidal morphologies, optical central surface brightnesses fainter than  $\sim 24 \text{ mag arcsec}^{-2}$ , and effective radii  $r_{\text{eff}} > 1.5 \text{ kpc}$ . While such objects have been known to exist for decades (e.g., Sandage & Binggeli 1984; Dalcanton et al. 1997; Conselice et al. 2003), their abundance in clusters was not fully appreciated. UDGs are now understood to be common in dense galaxy environments (e.g., van der Burg et al. 2016, 2017).

More recently, a population of gas-rich, blue UDGs with irregular morphologies has been uncovered in low-density environments (e.g., Bellazzini et al. 2017; Leisman et al. 2017; Román & Trujillo 2017a, 2017b; Trujillo et al. 2017; Greco et al. 2018).

Most known isolated UDGs have been discovered via neutral hydrogen gas (HI) using the ALFALFA survey (Giovanelli et al. 2005; Leisman et al. 2017); these objects are therefore generally gas-rich and star-forming. Two interesting exceptions are the optically discovered objects R-127-1 and M-161-1 (Dalcanton et al. 1997). Both of these galaxies are very isolated, yet they have quiescent optical spectra and low HI content (Papastergis et al. 2017). That they are both quenched and isolated is quite surprising, as essentially all known quenched dwarfs exist near a massive ( $M_{\star} \gtrsim 10^{10} M_{\odot}$ ) neighbor (Geha et al. 2012). This highlights the need for complete optically selected galaxy samples at low surface brightness, which complement HI searches that are biased to the most gas-rich systems. Indeed, a combination of deep optical and HI LSB galaxy surveys will be required to properly address pressing small-scale problems in standard cosmology such as the potential “too big to fail” problem (Boylan-Kolchin et al. 2011) in the field (Papastergis et al. 2015).

With this motivation, we are carrying out a blind search for LSB galaxies with the Hyper Suprime-Cam Subaru Strategic Program (HSC-SSP; Aihara et al. 2018a), an ongoing optical wide-field survey using the Hyper Suprime-Cam (Furusawa et al. 2018; Komiyama et al. 2018; Miyazaki et al. 2018; S. Kawanomoto et al. 2018, in preparation) on the Subaru Telescope. In our initial search of the first  $200 \text{ deg}^2$  of the survey (Greco et al. 2018), we uncovered  $\sim 800$  LSB galaxies,

spanning a wide range of galaxy colors and environments. Our survey is deep ( $5\sigma$  point-source detection of  $i \sim 26$  mag), wide ( $1400 \text{ deg}^2$  upon survey completion), and based on stellar continuum rather than gas, making it sensitive to both quenched and star-forming LSB galaxies.

As we show in Greco et al. (2018), our sample is diverse, ranging from dwarf spheroidals and UDGs in nearby groups to gas-rich irregulars to giant LSB spirals. To place our sample within the cosmological context, distance information will be essential. Therefore, we are undertaking a systematic follow-up program to map out the spatial distribution and physical properties of these galaxies. In this work, we present the results of a pilot study in which we obtained optical spectra of two galaxies (LSBG-285 and LSBG-750) from our sample, both of which turn out to be isolated, physically large ( $r_{\text{eff}} > 1 \text{ kpc}$ ) star-forming LSB dwarfs. These are the first two objects for which we have obtained spectroscopy, and they demonstrate that the HSC-SSP is sensitive to diffuse dwarf galaxies well beyond the Local Volume.

We organize this paper as follows. In Section 2, we describe our target selection for this pilot study. We present our spectroscopic data and analysis in Section 3 and our photometric data and analysis in Section 4. In Section 5, we present the physical and environmental properties of LSBG-285 and LSBG-750, and in Section 6 we discuss these objects in the context of the general dwarf galaxy and UDG populations. We conclude with a summary in Section 7.

Throughout this work, we assume a standard cosmology with  $H_0 = 70 \text{ km Mpc}^{-1}$ ,  $\Omega_m = 0.3$ , and  $\Omega_\Lambda = 0.7$ . All magnitudes presented in this paper use the AB system (Oke & Gunn 1983). Unless stated otherwise, we correct for Galactic extinction using the  $E(B - V)$  values from the dust map of Schlegel et al. (1998) and the recalibration from Schlafly & Finkbeiner (2011).

## 2. Target Selection

The target galaxies were discovered as part of a systematic search for LSB galaxies within the wide layer of the HSC-SSP (Greco et al. 2018). An overview of the HSC-SSP survey design is given in Aihara et al. (2018a), and the first public data release covering  $\sim 100 \text{ deg}^2$  is described in Aihara et al. (2018b). The Greco et al. (2018) galaxy sample contains  $\sim 800$  galaxies, roughly half of which are ultra-LSB, with  $g$ -band central surface brightnesses  $\mu_0(g) > 24 \text{ mag arcsec}^{-2}$ . The sample spans a wide range of galaxy colors and morphologies, with  $\sim 40\%$  of sources having blue optical colors ( $g-i < 0.7$ ) and ultraviolet (UV) detections in the *Galaxy Evolution Explorer* (GALEX) source catalog (Martin et al. 2005). This suggests ongoing star formation in these systems and makes them promising targets for follow-up emission-line measurements.

To test the feasibility of obtaining emission-line redshifts of such diffuse targets with a modest amount of telescope time, we selected three of the brightest UV sources from the Greco et al. (2018) sample that were visible from Gemini South during the Gemini Fast Turnaround 2017A semester for follow-up spectroscopic observations. Two of our selected targets were observed (LSBG-285 and LSBG-750), but the third became inaccessible from Gemini South before the observations could be taken. In Figure 1, we show HSC-SSP *gri* and GALEX far-UV (FUV)+near-UV (NUV) composite images of our two observed targets (our imaging data are described in Section 4).

## 3. Spectroscopic Data and Analysis

### 3.1. Observations and Data Reduction

We carried out long-slit spectroscopy of LSBG-285 and LSBG-750 on 2017 July 3 and 13, respectively, using the Gemini Multi-Object Spectrograph (GMOS) on Gemini South under Gemini Science Program GS-2017A-FT-21. Our primary goal was to measure redshifts and line ratios for our targets, rather than to spectrally or spatially resolve the emission-line kinematics. We used the  $831 \text{ line mm}^{-1}$  grating with a wide  $2''$  slit to increase our sensitivity for these LSB objects and to increase the probability of including H II regions within these galaxies. This configuration produced a spectral resolution of  $\sigma \approx 3 \text{ \AA}$ , which corresponds to  $140 \text{ km s}^{-1}$  at a wavelength of  $\lambda = 6563 \text{ \AA}$ , with an observed spectral range of  $4880\text{--}7200 \text{ \AA}$ .

To increase the per-pixel signal-to-noise ratio, we binned by four pixels in both the spatial and spectral directions, producing a pixel scale of  $0''.3$  in the spatial direction and  $1.5 \text{ \AA}$  in the spectral direction. For each source, the slit was centered on the galaxy and oriented along its major axis according to the parameters given in Greco et al. (2018); the slit positions are overlaid on the HSC-SSP images in Figure 1. The on-source integration time for each target was 1 hr.

We constructed a master bias by median-combining the evening's calibration bias frames and subtracting the overscan region. Flat fields were constructed by median-combining our observation-specific flat fields, subtracting the master bias, and applying the appropriate GMOS hot pixel mask provided by Gemini. Each target was observed for 20 minutes in three exposures. These individual exposures were bias-subtracted and then flat-fielded using our master flat. A gain normalization was applied to the individual CCDs, which were mosaicked into a single image for each exposure. The three exposures were finally combined into an individual image. Cosmic rays were removed using a median filter. We applied the same reduction methodology to the standard-star frames.

We used the arc spectra to apply an approximate wavelength solution to the combined target and standard-star mosaicked images and then used the positions of the night-sky lines to further improve the wavelength solution. Since there are few night-sky lines in the blue region of our spectra, the precision of the wavelength solution is a function of wavelength, with the highest precision occurring near H $\alpha$ . The rms errors about the wavelength solution were  $\sim 2.0$ ,  $0.4$ , and  $0.5 \text{ \AA}$  at  $\sim 5000$ ,  $6000$ , and  $7000 \text{ \AA}$ , respectively. We subtracted the average background using spectra on either side of the dispersed target spectrum that were free from emission due to sources that serendipitously fell within the slit. The target spectra were then flux-calibrated using spectra extracted from the mosaicked standard star.

We extracted 1D source spectra extending across the full spatial extent of the galaxies within rectangular regions, with lengths of 51 pixels ( $15''.3$ ) and 88 pixels ( $26''.4$ ) for LSBG-285 and LSBG-750, respectively. We further extracted subregions in the spatial direction with lengths of 17 pixels ( $5''.1 \approx 0.6 \text{ kpc}$ ) for LSBG-285 and 11 pixels ( $3''.3 \approx 0.6 \text{ kpc}$ ) for LSBG-750 to measure changes in the emission features as a function of position. In Figure 2, we show 2D and 1D spectra of each source.

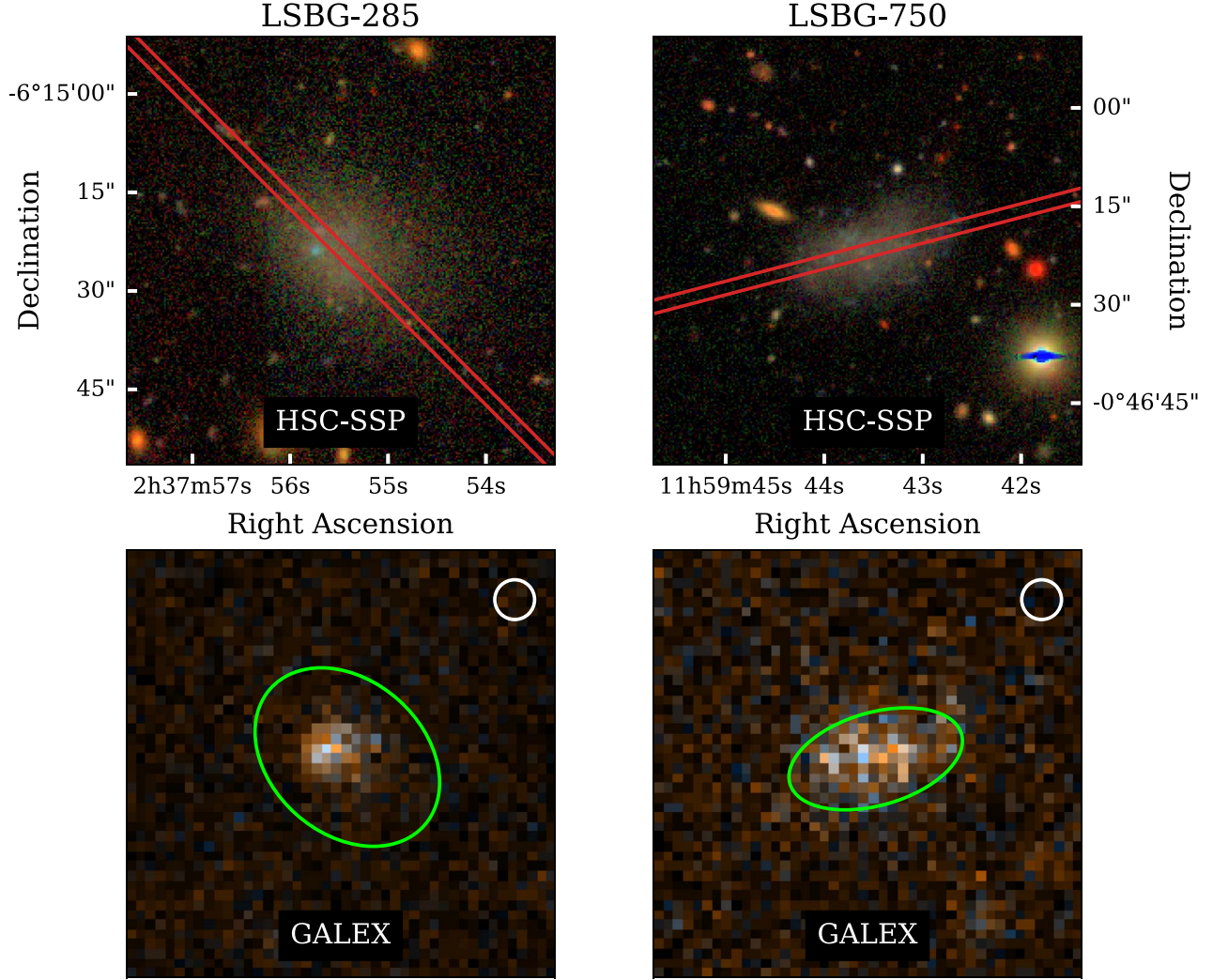


**Figure 1.** HSC-SSP *gri* (top row; Lupton et al. 2004) and *GALEX* FUV+NUV (bottom row) composite images of LSBG-285 (left column) and LSBG-750 (right column). In each HSC-SSP panel, the red lines show the slit position (Section 3.1). In each *GALEX* panel, the green ellipse shows the photometric aperture used in our SED fits (Section 4.2), and the white circle shows the approximate scale of the *GALEX* PSF. All of the images are 65'' on a side.

### 3.2. Emission-line Measurements

Our goal is to recover redshifts and line ratios from the extracted 1D spectra. For each galaxy, we perform the following analysis on the individual 0.6 kpc extractions, as well as the full galaxy extractions, which can be viewed as stacking the individual extractions to produce higher signal-to-noise ratio measurements.

We fit the  $H\alpha$  +  $[N II] \lambda\lambda 6549, 6583$  and  $[O III] \lambda 5007$  regions of each spectrum separately. For the former, we simultaneously fit the data with a flat continuum plus three Gaussian line profiles; since the lines are unresolved, we force the profiles to have the same width. We assume that the  $H\alpha$ - and  $[N II]$ -emitting regions are at the same redshift, with the redshift measurement being dominated by the much stronger  $H\alpha$  emission line. We further force the amplitude of  $[N II] \lambda 6549$  to be a factor of three below that of  $[N II] \lambda 6583$ .

Thus, our model of the  $H\alpha$  +  $[N II] \lambda\lambda 6549, 6583$  lines has five free parameters: two Gaussian amplitudes, one central wavelength, one profile width, and a constant. When fitting the  $[O III] \lambda 5007$  line, we assume a flat continuum plus a single Gaussian line profile with standard deviation given by the  $H\alpha$

fit, resulting in three free parameters. Note that the spectra do not cover  $[O III] \lambda 4959$  or  $H\beta$ .

To perform the fits, we assume independent Gaussian uncertainties and construct the standard log-likelihood function  $\ln \mathcal{L} \equiv -\chi^2/2$ . We first maximize the log-likelihood using L-BFGS-B optimization implemented in the *scipy* software package. The resulting maximum likelihood parameters are then used as the initialization of a Markov chain Monte Carlo (MCMC) exploration of the posterior probability distribution, where we assume reasonable (e.g., positive amplitudes), uniform proper priors on each parameter. For the MCMC implementation, we use *emcee* (Foreman-Mackey et al. 2013). In Figure 2, we show our best-fit models overlaid on each spectral extraction from LSBG-285 and LSBG-750.

The median  $[N II] \lambda 6583/H\alpha$  flux ratio and the associated 16th and 84th percentile uncertainties are indicated next to each spectrum in the relevant panel. In some cases, the detection of  $[N II] \lambda 6583$  is marginal, making the flux ratio highly uncertain. This is particularly true for the LSBG-750 spectra, which have a gap near the  $[N II] \lambda 6583$  line owing to a CCD artifact. Nevertheless, the full extractions, as well as some of the 0.6 kpc extractions, from both galaxies show statistically significant



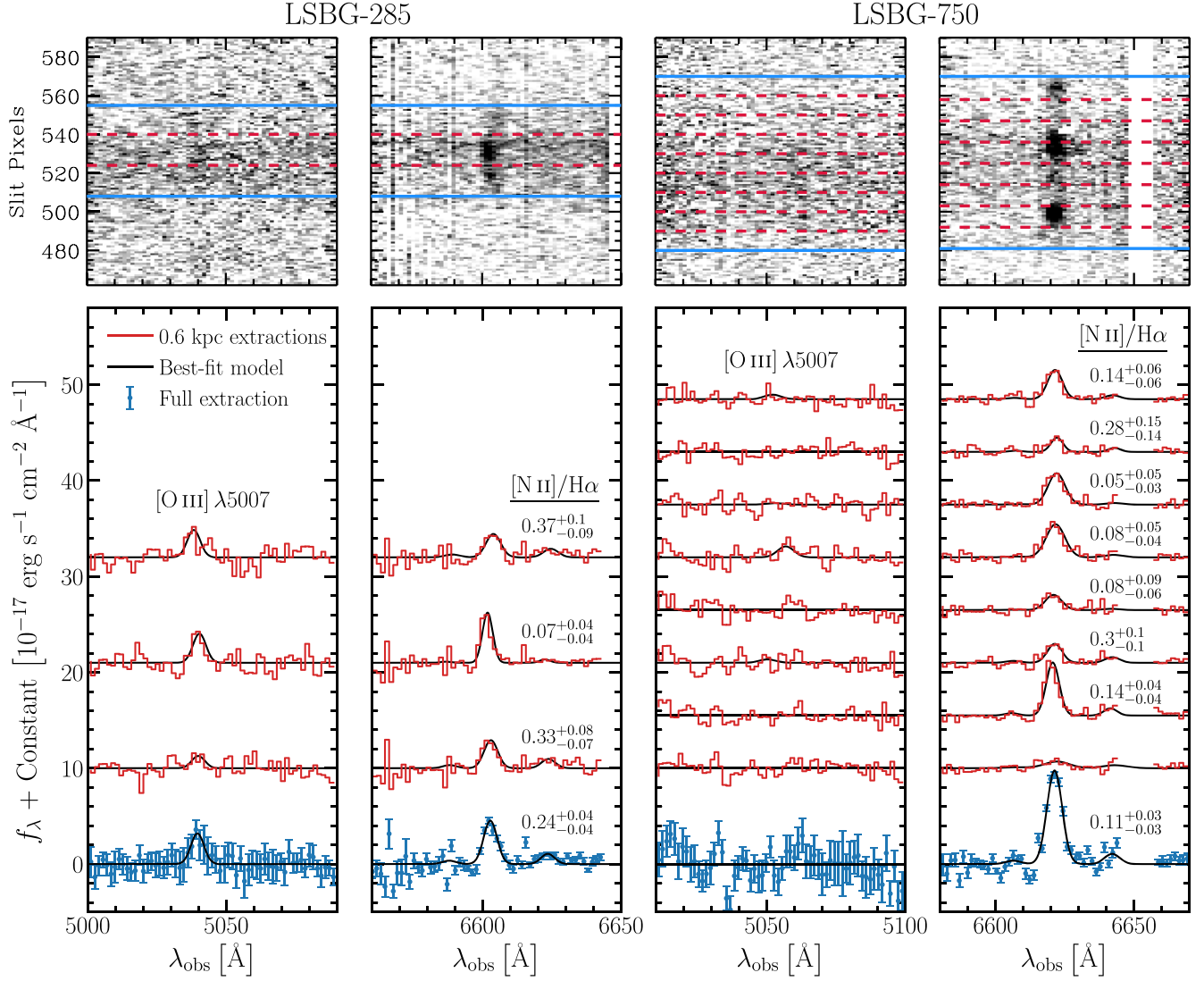


**Figure 2.** 2D (top) and 1D (bottom) spectra of LSBG-285 (left) and LSBG-750 (right). Red lines show individual 0.6 kpc extractions, and blue points show the full galaxy extraction. The red 1D spectra have been scaled by a factor of two for visibility. The best-fit spectral-line models (Section 3.2) are indicated by the black lines. The median  $[\text{N II}] \lambda 6583/\text{H}\alpha$  value and associated 16th and 84th percentile uncertainties, which we derive from the marginalized posterior probability distributions, are indicated near each spectrum in the relevant panels.

detections of  $[\text{N II}] \lambda 6583$ . We only detect  $[\text{O III}] \lambda 5007$  with a signal-to-noise ratio greater than 2.5 in two out of three of LSBG-285’s 0.6 kpc spectral extractions; this line is robustly detected in the full extraction of this galaxy. For all other cases, we calculate an upper limit for the  $[\text{O III}] \lambda 5007$  flux as  $\sqrt{2\pi} \sigma \times \text{median (pixel-to-pixel flux error)}$ , where  $\sigma$  is the width of the  $\text{H}\alpha$  line. All  $[\text{O III}] \lambda 5007$  measurements for LSBG-750 are upper limits.

Within the full galaxy spectral extractions for LSBG-285 and LSBG-750, the integrated  $\text{H}\alpha$  fluxes are  $\log(F_{\text{H}\alpha}/\text{erg cm}^{-2} \text{s}^{-1}) = -15.56 \pm 0.03$  and  $-15.17 \pm 0.01$ , respectively. For LSBG-285, the integrated  $[\text{O III}] \lambda 5007$  flux is  $\log(F_{\text{O III}}/\text{erg cm}^{-2} \text{s}^{-1}) = -15.7 \pm 0.1$ . These integrated fluxes have not been corrected for Galactic extinction.

### 3.3. Redshift and Distance Measurements

For our redshift measurements, we use the  $\text{H}\alpha$  emission line centroid detected in the full galaxy spectral extractions. LSBG-285 and LSBG-750 are diffuse dwarf galaxies outside of the

Local Volume, with redshifts of  $cz_{\text{helio}} = 1742 \pm 19 \text{ km s}^{-1}$  and  $cz_{\text{helio}} = 2586 \pm 18 \text{ km s}^{-1}$ , respectively, where the uncertainties are dominated by our wavelength calibration uncertainty. Given the relatively low recession velocities of these galaxies, we calculate distances using the local velocity field model of Mould et al. (2000), which accounts for the influence of the Virgo Cluster, the Great Attractor, and the Shapley Supercluster. For LSBG-285, we find a velocity correction of  $\delta v = -20.5 \text{ km s}^{-1}$ , and for LSBG-750, we find  $\delta v = 309 \text{ km s}^{-1}$ . The derived proper distances are  $24.6 \pm 0.3 \text{ Mpc}$  and  $41.3 \pm 0.3 \text{ Mpc}$ , respectively, where the quoted uncertainties only account for our redshift uncertainties.

## 4. Photometric Data and Analysis

### 4.1. Data Sets and Image Processing

We study the spectral energy distributions (SEDs) of our sources from the FUV to the mid-infrared (MIR) using archival NUV and FUV imaging from *GALEX*, *grizy* imaging from the

wide layer of HSC-SSP, and archival W1 ( $3.4\ \mu\text{m}$ ) imaging from the *Wide-field Infrared Survey Explorer* (WISE). Here we describe each data set and our procedure for obtaining/constructing the associated intensity and variance images, which we use to perform aperture photometry.

#### 4.1.1. GALEX

Both LSBG-285 and LSBG-750 serendipitously fell within archival *GALEX* pointings. For LSBG-285, we use imaging from *GALEX*'s Nearby Galaxy Survey with an exposure time of 1615 s in both the NUV and FUV filters. The imaging of LSBG-750 was taken as part of a *GALEX* Guest Investigator Program with an exposure time of 1549.5 s in both UV filters. For each galaxy, we downloaded the raw count ( $C$ ) and high-resolution relative response ( $R$ ) images from the Mikulski Archive for Space Telescopes *GALEX* tile retrieval service.<sup>6</sup> The intensity and variance images are then given by

$$I = C/R \text{ and } V = C/R^2. \quad (1)$$

Note that the *GALEX* intensity images are not background subtracted. We estimate the background in an annulus around each source during the aperture photometry procedure described below.

For the *GALEX* photometry, we estimate the Galactic reddening  $E(B - V)$  using the maps of Schlegel et al. (1998) and the Cardelli et al. (1989) extinction law with  $R_V = A_V/E(B - V) = 3.1$ ,  $A_{\text{FUV}} = 8.24 E(B - V)$ , and  $A_{\text{NUV}} = 8.2 E(B - V)$  (Wyder et al. 2007).

#### 4.1.2. HSC-SSP

We use *grizy* HSC-SSP imaging from the wide survey layer of the S16A internal data release (see Aihara et al. 2018b for information about HSC-SSP data releases). We directly use the data products produced by the HSC-SSP software pipeline (Bosch et al. 2018). These products include the background-subtracted intensity images, variance images, object masks, and the model point-spread function (PSF) at the location of each galaxy.

#### 4.1.3. unWISE

We use archival imaging from *WISE* (Wright et al. 2010) to constrain the MIR flux of the galaxy SEDs, which provides a strong constraint on internal extinction. The ALLWISE Atlas Images were PSF convolved by the *WISE* team to produce optimal detection maps, which degraded the native resolution of the images from  $\text{FWHM} \sim 6''.5$  to  $\text{FWHM} \sim 8''$ . Resolution is important for our aperture photometry measurements, since there is a large uncertainty associated with masking background sources that may dominate the light in a given aperture, particularly given the LSB nature of our sources. Therefore, we use the “unWISE” co-adds from Lang (2014), which preserve the resolution of the original *WISE* images. We downloaded background-subtracted intensity and variance cutout images of each source from the unWISE website.<sup>7</sup>

We inspected both the W1- and W2-band images, and the sources are visible in both bands. However, the detections in W2 are much noisier and likely suffer from oversubtraction (as evidenced by many negative pixels), particularly around

LSBG-285. Furthermore, the resolution of W1 is slightly better than that of W2. We therefore choose to exclude W2 from our analysis, noting that including it does not significantly impact any of our results.

We attempted to use the newest unWISE co-adds, which are based on the Near Earth Object (NEO) *WISE* Reactivation mission (Meisner et al. 2017a, 2017b). These co-adds reach a depth of coverage  $\sim 3\times$  greater than that of the AllWISE Atlas co-adds from Lang (2014), making them potentially better suited for this work. However, we found that our measured uncertainties on the resulting photometry were unreasonably small for both objects, and the W1 flux for both objects was significantly higher than the ALLWISE stacks. This behavior is consistent with previously known sky-subtraction problems with the NEOWISE co-adds, and it is recommended to use the original unWISE co-adds despite their having larger background noise than the newer ones that incorporate additional NEOWISE data (A. M. Meisner 2018, private communication).

#### 4.2. Aperture Photometry

Our goal is to measure the relative flux in each band within the same physical aperture; we do not attempt to capture all the galaxy light, which would be highly sensitive to the masking of background sources. We use elliptical apertures with parameters based on the catalog of Greco et al. (2018). To find the aperture size, we determine the radius at which the slope of the growth curve begins to rapidly increase owing to background sources entering the aperture. For each object, an aperture with semimajor axis equal to  $1.5 \times r_{\text{eff}}$  provides a good balance between capturing as much light as possible while avoiding the need to mask background sources; LSBG-285 has  $r_{\text{eff}} = 10''.3$ , and LSBG-750 has  $r_{\text{eff}} = 9''.0$ . These apertures are shown on the *GALEX* images in Figure 1. We note that the optical colors measured within these apertures are consistent at the  $\sim 0.01$  mag level with the colors based on the total model magnitudes measured by Greco et al. (2018).

To ensure that we are measuring light from the same physical components of the galaxies, we match the resolution of each image to that of the *WISE* W1 band, which has the broadest PSF ( $\text{FWHM} \sim 6''.5$ ). For the unWISE and *GALEX* images, we transform the PSFs to a Gaussian of width  $\text{FWHM} \sim 6''.5$  using the convolution kernels provided by Aniano et al. (2011). For the HSC-SSP images, we assume Gaussian PSFs and smooth each image with a Gaussian with standard deviation

$$\sigma = \sqrt{\sigma_{\text{target}}^2 - \sigma_{\text{intr}}^2}, \quad (2)$$

where  $\sigma_{\text{intr}}$  is the intrinsic resolution as measured by fitting a Gaussian to the model PSF at the location of each galaxy, and the target resolution is given by  $2\sqrt{2\ln 2} \sigma_{\text{target}} = 6''.5$ . To propagate the uncertainties from the image convolutions, we convolve each variance image with the square of the kernel used on the associated intensity image.

The photometric measurements are then given by

$$F = \sum_i \tilde{I}_i, \quad (3)$$

$$\sigma_F^2 = \sum_i \tilde{V}_i, \quad (4)$$

<sup>6</sup> <http://galex.stsci.edu>

<sup>7</sup> <http://unwise.me>

**Table 1**  
Matched-aperture Magnitudes

Filter	LSBG-285	LSBG-750
NUV	20.66 $\pm$ 0.09	20.52 $\pm$ 0.07
FUV	20.26 $\pm$ 0.06	20.31 $\pm$ 0.05
<i>g</i>	18.29 $\pm$ 0.08	19.00 $\pm$ 0.08
<i>r</i>	17.89 $\pm$ 0.08	18.77 $\pm$ 0.08
<i>i</i>	17.75 $\pm$ 0.08	18.69 $\pm$ 0.08
<i>z</i>	17.70 $\pm$ 0.09	18.62 $\pm$ 0.09
<i>y</i>	17.7 $\pm$ 0.1	18.6 $\pm$ 0.1
W1	19.1 $\pm$ 0.1	19.9 $\pm$ 0.2

**Note.** All magnitudes are on the AB system and have been corrected for Galactic extinction.

where the sum is over the pixels in the aperture,  $F$  is the measured flux,  $\sigma_F$  is the associated error estimate, and the tildes indicate that these are the images after the convolutions described above. We carry out these photometric measurements using the Astropy-affiliated package `photutils` (Bradley et al. 2017).

As noted in Section 4.1.1, the *GALEX* images have not been background subtracted. We therefore subtract a background level estimated within an annulus of inner radius  $4r_{\text{eff}}$  and outer radius  $7r_{\text{eff}}$  for each galaxy, with the appropriate error propagation term added to the variance. For the HSC-SSP photometry, Greco et al. (2018) estimate a typical uncertainty of 0.08 mag associated with sky subtraction near these sources, which we add to our HSC-SSP error estimates. We tabulate our matched-aperture photometric measurements in Table 1.

### 4.3. SED Fitting

We study the FUV–MIR SED of each galaxy using the aperture photometry from Section 4.2 and the Bayesian inference code `prospector`<sup>8</sup> (Johnson & Leja 2017). This software generates model SEDs on the fly using the Flexible Stellar Population Synthesis package (FSPS; Conroy et al. 2009) and explores the potentially high-dimensional posterior probability distribution via MCMC sampling. We run FSPS using the Calzetti et al. (2000) extinction curve, the MILES spectral templates (Sánchez-Blázquez et al. 2006; Falcón-Barroso et al. 2011), and the Padova isochrones (Marigo & Girardi 2007; Marigo et al. 2008). We implement MCMC using `emcee`. See Leja et al. (2017) and Pandya et al. (2018) for other applications of `prospector`.

Most of the parameters of FSPS may be free parameters in `prospector`. Our fiducial model assumes an exponentially declining star formation history ( $\tau$  model). We fix the source redshifts at their observed values and allow five parameters to float: stellar mass  $M_*$ , stellar metallicity  $Z_*$ , age since the first onset of star formation  $t_{\text{age}}$ ,  $e$ -folding timescale  $\tau$ , and internal extinction as parameterized by the  $V$ -band extinction coefficient  $A_V$ . All other parameters are fixed at their default values.<sup>9</sup> For comparison purposes, we also run the analysis with a simple stellar population (SSP;  $\tau = 0$  Gyr), as well as a dust-free model ( $A_V = 0$ ). We assume the following uniform priors:  $M_* = 10^6$  to  $10^{10} M_\odot$ ,  $[Z_*/Z_\odot] = -2.0$  to  $0.2$ ,  $\log_{10}(\tau/\text{Gyr}) = -1.0$  to  $1.0$ ,  $\log_{10}(t_{\text{age}}/\text{Gyr}) = -3.0$  to  $1.15$ , and  $A_V = 0$  to  $4$ .

We sample logarithmically in  $\tau$  and  $t_{\text{age}}$  and linearly in all other parameters.

Hydrodynamic cosmological simulations suggest that extended dwarf galaxies may have undergone bursty star formation histories (e.g., Di Cintio et al. 2017; Chan et al. 2018). However, it is difficult to observationally distinguish a smoothly declining star formation history from a bursty, episodic one (Ruiz-Lara et al. 2018). This is particularly true for a photometric SED analysis such as we present here. As a test, we ran our full analysis assuming a single-burst scenario combined with a  $\tau$  model, and the inferred parameters are very similar to our simpler fiducial model.

In Figure 3, we show our photometric measurements and the maximum a posteriori model spectra from our various `prospector` runs. We also show the marginalized parameter distributions for each case. Both SEDs are consistent with very little to no dust, regardless of whether we assume our fiducial  $\tau$ -model star formation history or an SSP, although the SSP does tend to predict higher  $A_V$  values (particularly for LSBG-750) to compensate for the lack of an older population of red stars. The marginalized parameter distributions for our models with and without dust are therefore very similar.

Focusing on our fiducial model, the stellar populations of both LSBG-285 and LSBG-750 are consistent with very low stellar metallicity ( $[Z_*/Z_\odot] < -1.0$ ) and intermediate age ( $t_{\text{age}} \approx 3$  and  $2$  Gyr), with extended star formation histories characterized by low  $e$ -folding timescales ( $\tau \approx 0.8$  and  $0.6$  Gyr). The  $\tau$  posterior distribution for both galaxies falls to very low values before it reaches  $\tau = 0.1$  Gyr (the boundary of our prior), suggesting that an exponentially declining star formation history is preferred over an SSP.

Compared to our fiducial  $\tau$  model, the SSP produces significantly different marginalized posterior distributions for the stellar mass, stellar metallicity, and age of the system. The SSP generally predicts stellar masses that are  $\sim 0.3$ – $0.5$  dex lower and ages that are  $\sim 0.6$ – $0.8$  dex lower than the  $\tau$  model. Furthermore, the marginalized distributions for the stellar metallicities become bimodal in the SSP case, with the metallicity posterior of LSBG-750 reaching to supersolar values.

The SSP results demonstrate the behavior of the marginalized posterior distributions in the limit that  $\tau \rightarrow 0$  Gyr. However, it is reasonable to assume that multiple generations of stars exist within these galaxies. In this scenario, the integrated light is easily dominated by the youngest stellar population, while the mass is dominated by somewhat older stars. For the remainder of the paper, we therefore assume the results from our fiducial  $\tau$  model, which are consistent with low, but nonzero,  $e$ -folding timescales  $\tau$ .

## 5. Galaxy Properties

We now combine results from our spectroscopic (Section 3) and photometric (Section 4) analyses to study the environments and physical properties of LSBG-285 and LSBG-750. A summary of the galaxy properties is provided in Table 2.

### 5.1. Environments

To investigate the galaxy environments, we search for neighbors using the NASA-Sloan Atlas<sup>10</sup> (NSA), which

<sup>8</sup> <https://github.com/bd-j/prospector>

<sup>9</sup> The default parameters are listed at <http://dfm.io/python-fsps>.

<sup>10</sup> <http://nsatlas.org>

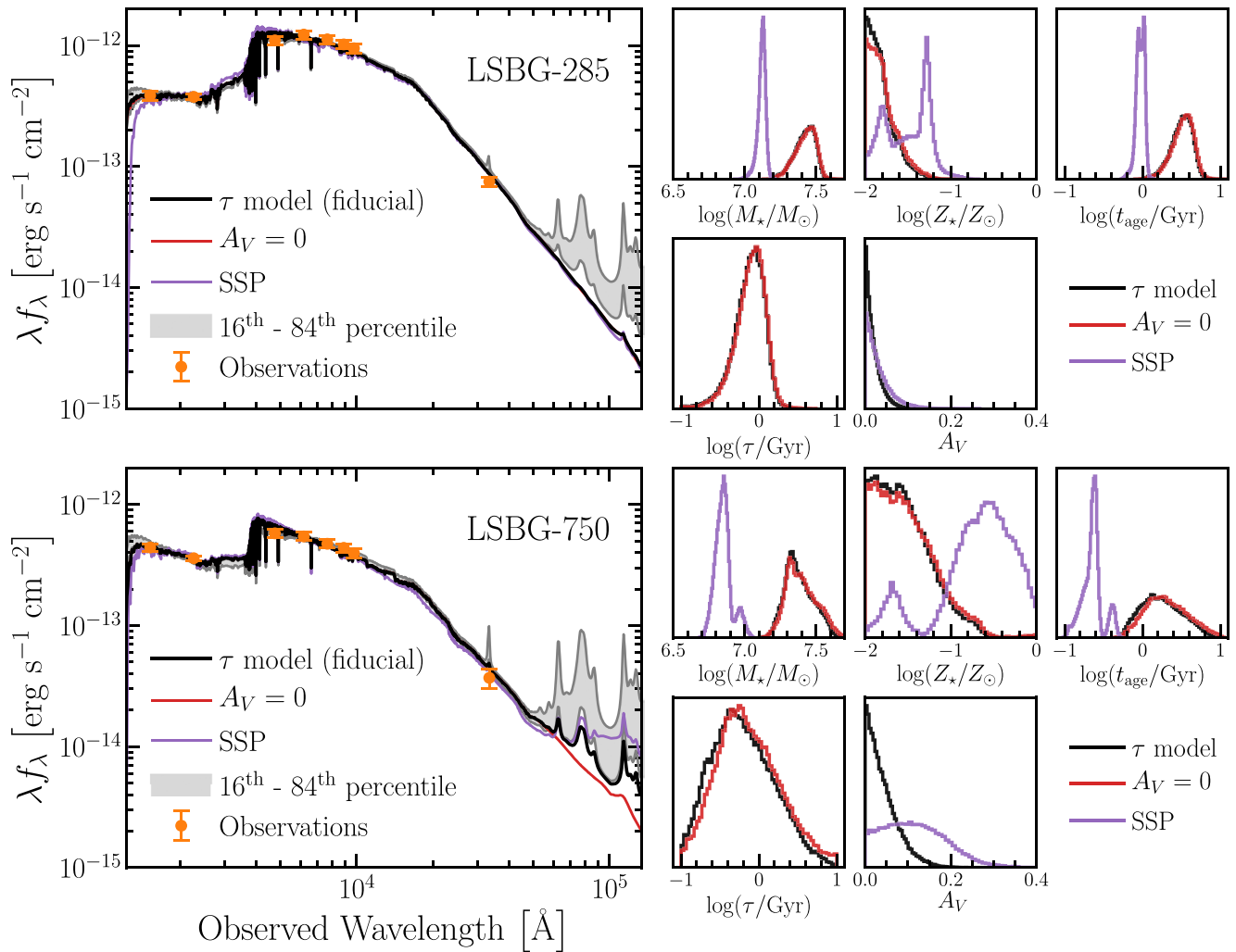


**Figure 3.** Left: observed photometry and the maximum a posteriori model spectra assuming a  $\tau$ -model star formation history with dust (our fiducial model), without dust ( $A_V = 0$ ), and a simple stellar population with dust (SSP;  $\tau = 0$ ). The gray shaded regions show the 16th–84th percentile  $\tau$ -model fluxes in each wavelength bin. Right: marginalized parameter distributions for each of the model assumptions shown in the left panel. We assume uniform priors for each parameter, with the bounds given in Section 4.3. The 50th percentile parameter values and the associated 16th and 84th percentile uncertainties are given in Table 2.

contains virtually all galaxies with known redshifts out to  $z = 0.055$  within the coverage of Sloan Digital Sky Survey (SDSS) DR8 (Aihara et al. 2011). The NSA also provides stellar mass estimates calculated using *kcorrect* (Blanton & Roweis 2007), which assumes the initial mass function of Chabrier (2003) and is based on fits to both the SDSS optical and, when available, *GALEX* fluxes.

Both LSBG-285 and LSBG-750 are quite isolated. Based on the NSA, LSBG-285’s nearest neighbor is a dwarf galaxy with  $M_* = 4 \times 10^7 M_{\odot}$  at a comoving separation of 1.2 Mpc, and the nearest galaxy with  $M_* > 10^{10} M_{\odot}$  is at a distance of 3.4 Mpc. Similarly, LSBG-750’s nearest neighbor is an  $M_* = 2 \times 10^7 M_{\odot}$  dwarf at a comoving separation of 1.6 Mpc, and the nearest galaxy with  $M_* > 10^{10} M_{\odot}$  is 4.5 Mpc away. For context, Geha et al. (2012) found that essentially all galaxies with  $M_* \lesssim 10^8 M_{\odot}$  that are separated by more than 1.5 Mpc from a massive host are star-forming, where massive hosts are defined to have  $M_* \sim 2.5 \times 10^{10} M_{\odot}$ . In other words, low-mass quenched galaxies only exist within a few virial radii of massive hosts. These authors define galaxies beyond 1.5 Mpc from a massive host to be in the field. The star-forming nature and isolation of our galaxies are consistent with

this picture. While both galaxies are in field-like environments, LSBG-750 is in a much lower density environment, with two galaxies with  $M_* > 10^7 M_{\odot}$  within 3 Mpc, whereas LSBG-285 has eight such dwarf galaxy neighbors (according to the NSA galaxy catalog).

The NSA catalog follows the footprint of SDSS DR8 and thus does not cover the entire sky. LSBG-285 and LSBG-750 fall 3°5 (1.5 Mpc) and 2°8 (2 Mpc) from the SDSS footprint boundary, respectively. Therefore, the most conservative statement about their environments is that they are at least these distances from a massive host. In the case of LSBG-285, the distribution of NSA galaxies around its location reflects the pattern of SDSS stripes, suggesting varying levels of completeness in this region. We searched the NASA/IPAC Extragalactic Database for neighbors around LSBG-285 that might be missing from the NSA galaxy catalog; no additional massive neighbors were found.

Our environment measures are prone to error owing to large relative velocities between the potential hosts and the target galaxies. Thus, as an additional measure of the isolation of these galaxies, we calculate their projected separations from all NSA galaxies with  $M_* = 2.5 \times 10^{10} M_{\odot}$  within a redshift



**Table 2**  
Galaxy Properties

Observed Property		LSBG-285	LSBG-750
R.A.	J2000	02 <sup>h</sup> 37 <sup>m</sup> 55. <sup>s</sup> 48	11 <sup>h</sup> 59 <sup>m</sup> 43. <sup>s</sup> 55
Decl.	J2000	−06°15′23″.86	−00°46′21″.76
$C_{\text{helio}}$	km s <sup>−1</sup>	1742 ± 19	2586 ± 18
$m_g$	mag	18.0 ± 0.2	18.6 ± 0.2
$\mu_0(g)$	mag arcsec <sup>−2</sup>	24.1 ± 0.4	24.2 ± 0.4
$g - r$	mag	0.4 ± 0.1	0.2 ± 0.1
$g - i$	mag	0.5 ± 0.1	0.3 ± 0.1
NUV − $r$	mag	2.37 ± 0.09	1.54 ± 0.09
$r_{\text{eff}}$	arcsec	10.3 ± 0.8	9.0 ± 0.8
Ellipticity		0.25 ± 0.03	0.48 ± 0.03
Sérsic $n$		0.7 ± 0.3	0.6 ± 0.3
Derived Property		LSBG-285	LSBG-750
Distance <sup>a</sup>	Mpc	24.6 ± 0.3	41.3 ± 0.3
$M_g$	mag	−14.0 ± 0.2	−14.5 ± 0.3
$r_{\text{eff}}$	kpc	1.2 ± 0.1	1.8 ± 0.2
$M_*$	10 <sup>7</sup> $M_\odot$	2.7 <sup>+0.4</sup> <sub>−0.5</sub>	2.3 <sup>+0.9</sup> <sub>−0.6</sub>
$A_V$	mag	<0.06	<0.11
$[Z_*/Z_\odot]^b$		<−1.5	<−1.0
$t_{\text{age}}^c$	Gyr	3.3 <sup>+1.0</sup> <sub>−0.9</sub>	1.7 <sup>+1.7</sup> <sub>−0.8</sub>
$\tau^d$	Gyr	0.8 <sup>+0.4</sup> <sub>−0.3</sub>	0.6 <sup>+1.0</sup> <sub>−0.3</sub>
12 + log(O/H) <sup>e</sup>		8.4 ± 0.2	8.4 ± 0.3

**Notes.** Coordinates, total magnitudes, surface brightnesses, and structural measurements are from Greco et al. (2018). All magnitudes are on the AB system, and they have been corrected for Galactic extinction using the dust map of Schlegel et al. (1998) and the recalibration from Schlafly & Finkbeiner (2011). Parameters inferred from our SED fits assume an exponentially declining star formation history, and we quote the median, 16th percentile, and 84th percentile of the marginalized posterior distributions. Upper limits are the 95th percentile of the posterior distributions. For distance-dependent quantities, we conservatively add in quadrature a systematic uncertainty equal to the difference between our adopted parameter value and the value derived from assuming pure Hubble flow.

<sup>a</sup> Distances assume the flow model of Mould et al. (2000). Quoted uncertainties only account for our redshift uncertainties.

<sup>b</sup> Stellar metallicity.

<sup>c</sup> Age since the first onset of star formation.

<sup>d</sup> Star formation history  $e$ -folding timescale.

<sup>e</sup> Median oxygen abundance of spectral extractions, where the error is the spread in values. The Sun has 12 + log(O/H) = 8.66.

range of  $|\Delta z| \cdot c = 500 \text{ km s}^{-1}$ . In this case, the nearest massive neighbors to LSBG-285 and LSBG-750 are at projected distances of 0.9 and 4.7 Mpc, respectively. Using this isolation metric, both galaxies are in low-density, field-like environments, and LSBG-750 in particular appears to be extremely isolated.

### 5.2. Stellar Masses and Effective Radii

The photometric apertures we used for SED fitting only contain a fraction of the total galaxy light. We therefore assume that the inferred stellar mass-to-light ratios are uniform with radius and use the total  $i$ -band magnitudes from Greco et al. (2018) to estimate the total stellar masses; these magnitudes are based on 2D Sérsic function fits to the HSC-SSP images. We find that LSBG-285 has  $M_* = 2.7 \times 10^7 M_\odot$  and LSBG-750 has  $M_* = 2.3 \times 10^7 M_\odot$ . To estimate the physical extent of these galaxies, we again use the single Sérsic function fits from Greco et al. (2018), finding that LSBG-285 and LSBG-750

have effective radii of  $r_{\text{eff}} = 1.2$  and 1.8 kpc, respectively. Hence, both are consistent with being  $\sim 10^7 M_\odot$  LSB dwarf galaxies at the small-size end of the UDG population.

These results are summarized in Table 2 as the 50th, 16th, and 84th percentiles of the marginalized posterior distributions shown in Figure 3. Since these galaxies are relatively nearby, their distances have added uncertainty due to the local velocity field. For all distance-dependent quantities in Table 2, we adopt the values inferred from assuming the Mould et al. (2000) flow model. For each of these parameters, we conservatively add in quadrature a systematic uncertainty equal to the difference between our adopted parameter value and the value derived from assuming pure Hubble flow.

### 5.3. Star Formation Rates (SFRs)

Assuming the distances we derived from the flow model of Mould et al. (2000), we calculate SFRs using the measured FUV luminosities and the scaling relation from Kennicutt (1998):

$$\text{SFR} [M_\odot \text{ yr}^{-1}] = \frac{L_\nu(\text{FUV})}{7.14 \times 10^{27} \text{ erg s}^{-1} \text{ Hz}^{-1}}, \quad (5)$$

where  $L_\nu(\text{FUV})$  is the Galactic-extinction-corrected FUV luminosity measured within an elliptical aperture with semimajor axis equal to  $2.5 \times r_{\text{eff}}$  for LSBG-285 and  $4 \times r_{\text{eff}}$  for LSBG-750. The inferred SFRs are  $\sim 0.002$  and  $0.009 M_\odot \text{ yr}^{-1}$ , respectively, where we have not corrected for internal extinction from dust. As our SED fits show (Section 4.3), both galaxies likely have  $A_V < 0.1$  mag. If we assume the 95th percentile upper limits on  $A_V$  given in Table 2 and the extinction law of Cardelli et al. (1989) with  $R_V = A_V/E(B - V) = 3.1$ , the FUV luminosity correction leads to SFRs that are higher by  $\sim 10\%$  for LSBG-285 and  $\sim 20\%$  for LSBG-750. In either case, these SFRs are low compared to gas-rich galaxies of similar stellar mass detected by ALFALFA (Huang et al. 2012), though they are consistent with the large scatter observed in this relation.

For normal spiral galaxies with  $\text{SFR} \sim 1 M_\odot \text{ yr}^{-1}$ , FUV-derived SFRs largely agree with those estimated from H $\alpha$  nebular emission after accounting for internal dust attenuation; however, for dwarf galaxies with  $\text{SFR} < 0.1 M_\odot \text{ yr}^{-1}$ , H $\alpha$  SFRs have been observed to systematically underpredict the total SFR relative to FUV SFRs (Lee et al. 2009). To test whether our sources follow this trend, we estimate the H $\alpha$  SFR as (Kennicutt 1998)

$$\text{SFR} [M_\odot \text{ yr}^{-1}] = \frac{L(\text{H}\alpha)}{1.26 \times 10^{41} \text{ erg s}^{-1}}, \quad (6)$$

where  $L(\text{H}\alpha)$  is the Galactic-extinction-corrected integrated H $\alpha$  luminosity. To compare the FUV and H $\alpha$  SFRs, we recalculate the FUV SFR using our smaller SED apertures and apply a rough aperture correction to  $L(\text{H}\alpha)$  given by the ratio of the areas of the photometric and spectral apertures. This assumes that the H $\alpha$  emission extends throughout the photometric apertures, which, given the patchiness seen in the 2D spectra, likely overestimates  $L(\text{H}\alpha)$  (particularly in the case of LSBG-285).

For LSBG-285, H $\alpha$  predicts a higher SFR than FUV, with  $\text{SFR}(\text{H}\alpha)/\text{SFR}(\text{FUV}) \sim 1.5$ . In contrast, for LSBG-750, the two SFRs are consistent, with  $\text{SFR}(\text{H}\alpha)/\text{SFR}(\text{FUV}) \sim 1$ . Both



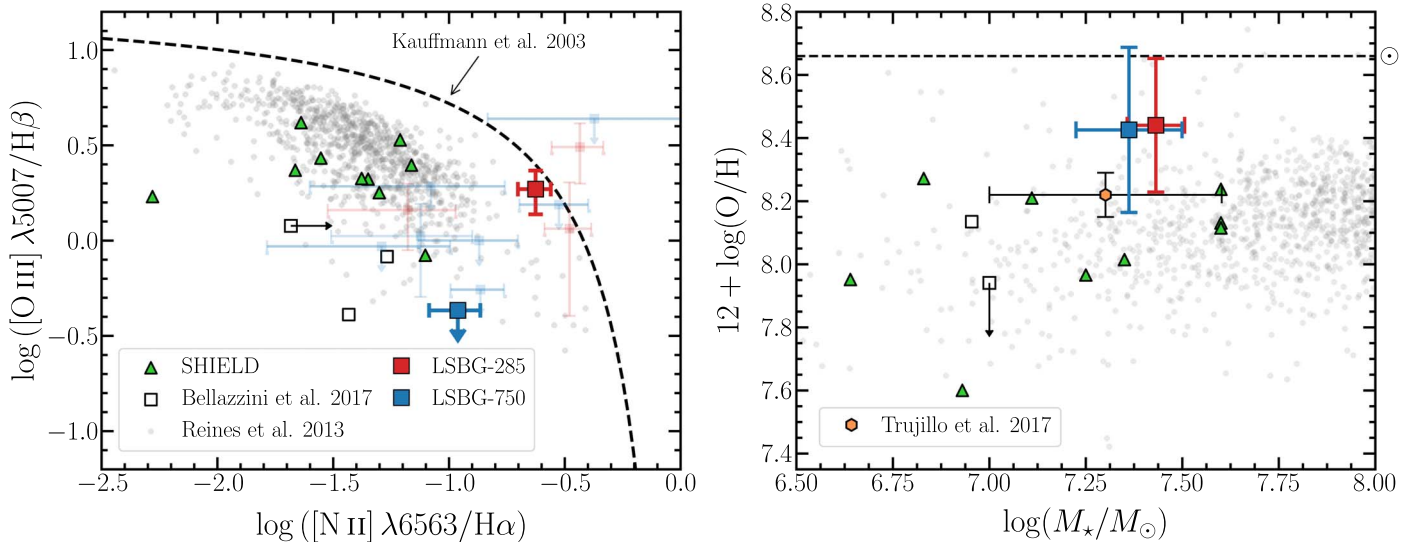


**Figure 4.** Left: emission-line diagnostic diagram based on our full galaxy spectral extractions (large filled squares) and individual 0.6 kpc extractions (small transparent squares). Upper/lower limits are indicated by arrows. The dashed curve divides the diagram into regions that are typically occupied by star-forming nebulae and active galactic nuclei (Kauffmann et al. 2003). We also show measurements from SHIELD galaxies (Haurberg et al. 2015), two extended dwarf irregulars (Bellazzini et al. 2017), and low-mass star-forming galaxies selected from the NSA by Reines et al. (2013). Right: oxygen abundance–stellar mass relation for the same samples as the left panel. The error bars for LSBG-285 and LSBG-750 show the spread in metallicity between the individual spectral extractions. In addition, the nearby star-forming UDG UGC 2162 (Trujillo et al. 2017) is indicated by the orange hexagon. Oxygen abundances were derived from the linear relation of Pettini & Pagel (2004). Solar abundance is indicated by the dashed black line.

of these values are consistent with the scatter observed in this ratio for galaxies of similar stellar mass and SFR (Lee et al. 2009). Note that these are very approximate calculations, particularly given the very uncertain aperture corrections for  $H\alpha$ .

#### 5.4. Gas-phase Metallicities

We robustly detect  $H\alpha$  in both LSBG-285 and LSBG-750. As described in Section 3.2, we also have marginal detections of  $[N II] \lambda 6583$  for both sources, suggesting that it may be possible to use the  $[N II] \lambda 6583/H\alpha$  flux ratio as a probe of gas-phase metallicity. However, we must first verify that the observed emission is consistent with being due to H II regions. For this purpose, we use the emission-line diagnostic diagram of Baldwin et al. (1981; the BPT diagram),  $[N II] \lambda 6583/H\alpha$  versus  $[O III] \lambda 5007/H\beta$ . While we have upper limits and/or detections of  $[O III] \lambda 5007$  in both objects,  $H\beta$  is outside the wavelength range of our observations. Nevertheless, our SED fitting results suggest that there is very little dust in these galaxies ( $A_V < 0.1$ ), making it reasonable to assume  $H\alpha/H\beta = 2.86$ . This is the intrinsic ratio corresponding to a temperature of  $10^4$  K and electron density of  $10^2 \text{ cm}^{-3}$  for case B recombination (Osterbrock 1989).

Assuming this value for  $H\alpha/H\beta$ , we show our sources on the BPT diagram in the left panel of Figure 4. Our full galaxy spectral extractions have the highest signal-to-noise ratio and are indicated by the red (LSBG-285) and blue (LSBG-750) filled squares. Our measurements within 0.6 kpc apertures are indicated by small transparent squares with error bars. The dashed curve divides this plane into regions expected to be occupied by star-forming nebulae and active galactic nuclei (Kauffmann et al. 2003). Within the uncertainties, all of our measurements confirm that LSBG-285 and LSBG-750 fall within the star-forming locus of the BPT diagram, as expected.

The gray points in Figure 4 show  $\sim 1000$  low-mass galaxies ( $M_* \sim 10^{6.5} - 10^8 M_\odot$ ) selected from the NSA galaxy catalog by

Reines et al. (2013), who were searching for active galactic nuclei in dwarf galaxies. The green triangles show measurements of H II regions in H I-selected dwarfs from the SHIELD project (Cannon et al. 2011; Haurberg et al. 2015). With H I masses as low as  $\sim 10^{6.5} M_\odot$ , the SHIELD galaxies were selected to sample the very low mass end of the H I mass function. We also show measurements from H II regions in two dwarf irregular galaxies (open squares) with UDG-like sizes and surface brightnesses (Bellazzini et al. 2017).

The measurements from our sources tend to have higher  $[N II] \lambda 6583/H\alpha$  and lower  $[O III] \lambda 5007/H\beta$  than most of the systems in Figure 4, albeit with large uncertainties in both flux ratios. This trend in the BPT diagram—moving down and to the right—is known to correlate with increasing gas-phase metallicity (e.g., Moustakas et al. 2006). In the right panel of Figure 4, we show oxygen abundance as a function of stellar mass for the same systems shown in the left panel. For each measurement, we calculate the oxygen abundance assuming the linear relation from Pettini & Pagel (2004):

$$12 + \log(O/H) = 8.9 + 0.57 N_2, \quad (7)$$

where  $N_2 \equiv \log([N II] \lambda 6583/H\alpha)$ . Both LSBG-285 and LSBG-750 are consistent with having high gas-phase metallicity for their stellar mass. The nearby star-forming UDG UGC 2162 also has a relatively high gas-phase metallicity for its stellar mass of  $\sim 2 \times 10^7 M_\odot$  (Trujillo et al. 2017); this object is indicated by the orange hexagon in the right panel of Figure 4. As we obtain more optical spectra of blue UDGs, both optically and H I selected, it will be interesting to see whether this trend continues.

It is important to note that the above results are tentative given the relatively low signal-to-noise ratio of our measurements and the uncertainties associated with applying Equation (7) to such diffuse systems. This relation was calibrated with samples of individual H II regions with direct-method metallicity measurements; however, diffuse ionized gas

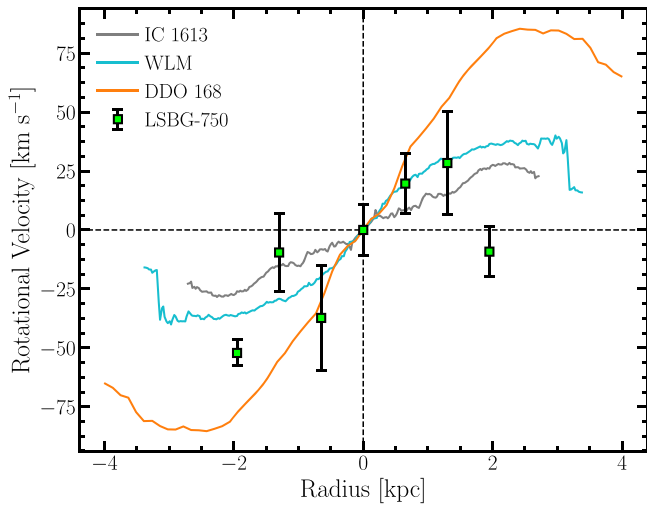


**Figure 5.** Evidence for ordered rotation in LSBG-750 with a maximum rotational velocity of  $\lesssim 50 \text{ km s}^{-1}$ . As a qualitative comparison, we show high-resolution H I rotation curves of dwarf galaxies with stellar masses of  $\sim 10^7$ – $10^8 M_\odot$ , which have estimated halo masses ranging from  $10^9 M_\odot$  (IC 1613) to  $10^{11} M_\odot$  (DDO 168; Oh et al. 2015). The velocities have been corrected for inclination.

not contained in H II regions also contributes significantly to the optical line emission of galaxies, and the addition of this component may lead to elevated [N II]  $\lambda 6583/\text{H}\alpha$  compared to single H II regions (Sanders et al. 2017), which would bias our metallicity estimate high. Finally, we note that galaxy samples (particularly optically selected samples) in this mass and surface brightness range are highly incomplete, so it is currently difficult to assess the significance of the above comparison.

### 5.5. Ordered Rotation in LSBG-750

As can be seen by careful inspection of Figure 2, the wavelength offsets of LSBG-750’s individual spectral extractions show some evidence of ordered rotation, whereas LSBG-285’s H $\alpha$ -emitting region is more concentrated (allowing three vs. eight extractions on the same physical scale) with offsets that are not consistent with rotation based on the current data. Our current data lack the signal-to-noise ratio needed to perform detailed mass modeling based on LSBG-750’s observed rotation curve. Nevertheless, in Figure 5 we make a qualitative comparison with high-resolution ( $\sim 6''$  angular and  $< 2.6 \text{ km s}^{-1}$  velocity resolution) H I rotation curves (Oh et al. 2015) of dwarf galaxies of similar stellar mass ( $\sim 10^7$ – $10^8 M_\odot$ ) from the LITTLE THINGS survey (Hunter et al. 2012). For LSBG-750, we assume the center of the H $\alpha$ -emitting region as the central position and velocity.

All the velocities have been corrected for inclination, where for LSBG-750 we use the ellipticity measured from the *i*-band image and assume that it is an oblate spheroid with an edge-on axis ratio of 0.2 (e.g., Holmberg 1958). We note that the ellipticity distribution of our full LSB galaxy catalog suggests that on average objects in our sample are intrinsically round (Greco et al. 2018). However, the above inclination correction will only increase the velocities, which for our purposes is the more conservative assumption.

For comparison, the dwarf galaxies IC 1613, WLM, and DDO 168 (Figure 5) have measured dynamical masses of  $\log(M_{\text{dyn}}/M_\odot) \sim 8.4, 9.0$ , and  $9.5$ , respectively (Oh et al. 2015).

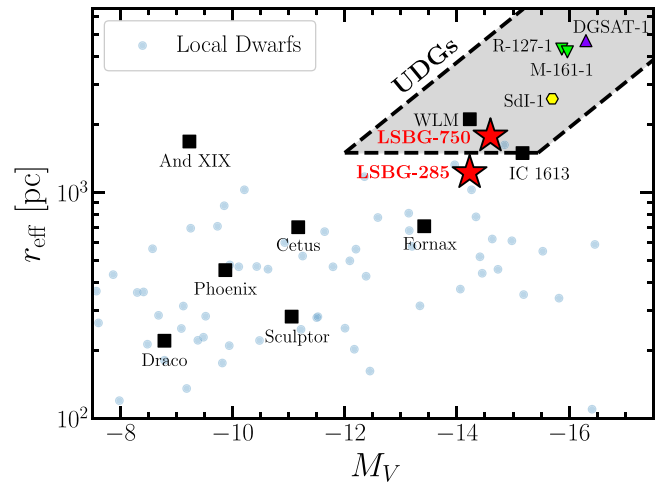


**Figure 6.** Size–luminosity relation for our two sources (red stars), dwarf galaxies in and around the Local Group (filled circles; McConnachie 2012), and ultradiffuse galaxies (UDGs; gray shaded region; van Dokkum et al. 2015) in low-density environments (Dalcanton et al. 1997; Martínez-Delgado et al. 2016; Bellazzini et al. 2017). The labeled black squares show well-known dwarf galaxies from the Local Group.

Based on the mass models of Oh et al. (2015), their estimated halo masses are  $\log(M_{\text{halo}}/M_\odot) \sim 9, 10$ , and  $11$ , respectively. The H $\alpha$ -emitting region in LSBG-750 roughly extends across the entire optical galaxy. The H I may extend beyond the H $\alpha$  in this galaxy, but there is often good agreement (at the level of our uncertainties) between H $\alpha$  and H I maximum rotational velocities in LSB galaxies (e.g., de Blok & Bosma 2002; Marchesini et al. 2002). We thus infer that LSBG-750 has a maximum rotational velocity  $\lesssim 50 \text{ km s}^{-1}$ , which corresponds to a dynamical mass of  $\lesssim 10^9 M_\odot$  at  $\sim 2 \text{ kpc}$ . At  $M_\star \sim 10^7 M_\odot$ , a rotational velocity of  $\sim 50 \text{ km s}^{-1}$  is relatively high, but it is consistent with the large scatter observed in the stellar mass Tully–Fisher relation (e.g., Torres-Flores et al. 2011; Bradford et al. 2016). Based on this upper limit and the qualitative comparison with similar objects in Figure 5, LSBG-750 likely occupies a dwarf-mass dark matter halo with  $M_{\text{halo}} < 10^{11} M_\odot$ . This result adds to the growing list of rotational measurements of blue (Leisman et al. 2017; Trujillo et al. 2017; Spekkens & Karunakaran 2018) and red (Ruiz-Lara et al. 2018) UDGs that are consistent with dwarf-like halo masses.

## 6. Discussion

The Greco et al. (2018) galaxy sample—from which LSBG-285 and LSBG-750 were selected—contains  $\sim 800$  LSB galaxies, and a significant fraction of these galaxies are blue and UV emitting. The present work is a pilot study for a more systematic follow-up effort to map out the spatial distribution and physical properties of this larger galaxy sample. The optical and environmentally blind selection of our diffuse-galaxy sample nicely complements most previous work, which generally covers small volumes (e.g., Dalcanton et al. 1997) and/or is biased by either environment (e.g., van Dokkum et al. 2015) or gas fraction (e.g., Leisman et al. 2017). Here we place the first two sources we have followed up in context with UDGs and the general dwarf galaxy population.

In Figure 6 we show LSBG-285 and LSBG-750 in the size–luminosity plane, along with dwarf galaxies in and around the Local Group (McConnachie 2012). We have labeled

well-known local dwarfs such as Sculptor (the prototypical dwarf spheroidal galaxy), Fornax, and the Wolf–Lundmark–Melotte (WLM) irregular galaxy. The shaded gray region shows roughly where UDGs fall within this parameter space (van Dokkum et al. 2015). We also show other known isolated UDGs such as the H I-rich SECCO-dI-1 (Bellazzini et al. 2017) and the intriguingly quiescent R-127-1 and M-161-1 (Dalcanton et al. 1997). SECCO-dI-2 (Bellazzini et al. 2017) is another example of an H I-rich, relatively isolated UDG, but it has similar size and luminosity to our sources and is not shown for clarity. DGSAT-1 (Martínez-Delgado et al. 2016) has a red color and exists in a filamentary region near the Pisces–Perseus supercluster with at least two  $M_* > 10^{10} M_\odot$  neighbors within 1 Mpc (Papastergis et al. 2017). Where necessary, we convert  $gr$  measurements to  $V$  band using the transformation  $V = g - 0.59(g-r) - 0.01$  (Jester et al. 2005).

We note that our full sample is not expected to contain many (if any) objects in the Local Volume (distances within  $\sim 10$  Mpc), since such nearby sources have very large sizes on the sky<sup>11</sup> (see Danieli et al. 2018 for a study of the discovery space for integrated-light searches for LSB dwarfs within the Local Volume). Nonetheless, we are finding field galaxies at the high end of the Local Group luminosity and size distributions. Andromeda XIX (And XIX), an M31 satellite, is an interesting object, as its large size for its luminosity is likely due to tidal interactions with its massive host (Collins et al. 2013). WLM and IC 1613 are two other well-known Local Volume objects with UDG-like luminosities and sizes; we compare the rotation curves of these sources with that of LSBG-750 in Figure 5. It is interesting to note that, in contrast to our sources and the isolated UDGs mentioned above, Local Volume UDG candidates identified in the Updated Nearby Galaxy Catalog (Karachentsev et al. 2013) appear to be associated exclusively with massive neighbors (Karachentsev et al. 2017).

For UDGs that exist in galaxy clusters or groups (e.g., Yagi et al. 2016; van der Burg et al. 2017), environmental processes such as ram pressure stripping may be responsible for their ultralow stellar densities (e.g., Yozin & Bekki 2015). In contrast, for isolated galaxies such as LSBG-285 and LSBG-750 (e.g., Dalcanton et al. 1997; Bellazzini et al. 2017), internal processes are required to explain their structural properties. In an H I follow-up study of four relatively isolated UDGs, Papastergis et al. (2017) found that they fell into two categories—one is H I rich and star-forming and the other is apparently gas-poor and quiescent.

Our sources likely fit into the former category. If they follow the stellar density–color–gas fraction relation from Huang et al. (2012), they are expected to have gas fractions of  $M_{\text{H I}}/M_* \sim 1.3\text{--}3.0$ . If this H I content is found, their extended star formation histories may be consistent with the formation scenario proposed by Di Cintio et al. (2017), in which feedback-induced outflows lead to the expansion of the dark matter and stellar distributions, and for isolated systems, a significant H I gas mass is predicted.

It is also possible that our sources represent the high-spin tail of the dwarf galaxy population (Amorisco & Loeb 2016), which in the case of LSBG-750 is also consistent with our data (Section 5.5); higher signal-to-noise ratio optical spectra

and/or H I kinematic measurements are necessary to properly test this scenario.

Similar to the few UDGs whose stellar populations have been studied spectroscopically (Gu et al. 2018; Kadowaki et al. 2017; Ferre-Mateu et al. 2018; Ruiz-Lara et al. 2018) and photometrically (Pandya et al. 2018), both our sources are consistent with the observed stellar mass–metallicity relation for dwarf galaxies (Kirby et al. 2013), which is roughly continuous with the relation for galaxies as massive as  $M_* = 10^{12} M_\odot$ . However, these previously studied UDGs are all quenched systems—LSBG-750 extends this relation to star-forming UDGs in the field with stellar masses in the  $\sim 10^7 M_\odot$  range. Whether or not there is an evolutionary link between blue and red UDGs remains an open question, though there are hints that such a link exists (e.g., Román & Trujillo 2017b).

The similar stellar mass–metallicity relation for cluster and field UDGs is at least consistent with these objects having similar formation histories, with differences due to environment occurring at late times. Furthermore, this supports the hypothesis that most UDGs are extensions of the general dwarf galaxy population. However, it is interesting that the gas-phase metallicities appear to be relatively high in our two sources and UGC 2162 (see Figure 4), all of which have relatively large physical sizes for their stellar mass. In particular, the opposite trend is observed in galaxies of higher stellar mass ( $M_* \gtrsim 5 \times 10^8 M_\odot$ ), where smaller sizes at fixed stellar mass correspond to higher gas-phase metallicities (e.g., Ellison et al. 2008; Sánchez Almeida & Dalla Vecchia 2018). While it is possible that the elevated metallicities in these diffuse systems are due to the deep gravitational potential wells of overmassive dark matter halos, as has been observed in a Coma UDG (van Dokkum et al. 2016; although see Di Cintio et al. 2017), the current rotational measurements of both LSBG-750 and UGC 2162 (Trujillo et al. 2017) point toward typical stellar-to-halo mass ratios for these galaxies. We again caution that there are large uncertainties associated with the  $[\text{N II}]\lambda 6583/\text{H}\alpha$ –oxygen abundance relation (Sanders et al. 2017), which we have used to infer the gas-phase metallicities.

Based on the redshifts we currently have in hand (both archival redshifts and those presented here) for galaxies in the Greco et al. (2018) sample, we are finding diffuse galaxies at distances in the range of  $\sim 20\text{--}200$  Mpc. Our follow-up program will therefore significantly expand the volume out to which it is possible to study optically selected, LSB dwarf galaxies. This effort, combined with complementary H I (e.g., Giovanelli et al. 2013; Tollerud et al. 2015) and optical (e.g., Danieli et al. 2018) searches for LSB dwarfs within the Local Volume, will provide a much more complete picture of the low-luminosity, LSB dwarf galaxy population, which will have important implications for our understanding of galaxy formation within the  $\Lambda$ CDM cosmological framework.

## 7. Summary

We have presented a follow-up study of two diffuse dwarf galaxies in the field, LSBG-285 and LSBG-750, which were recently discovered with the HSC-SSP (Greco et al. 2018). These galaxies live outside the Local Volume at comoving distances of  $\approx 25$  and  $\approx 41$  Mpc, respectively. There are no massive galaxies ( $M_* > 10^{10} M_\odot$ ) within at least 1.5 Mpc from LSBG-285 and 2 Mpc from LSBG-750. Both objects are physically large compared to most dwarfs in and around the Local Group (Figure 6); LSBG-285 has  $r_{\text{eff}} = 1.2$  kpc and

<sup>11</sup> Our search was carried out on  $12' \times 12'$  patches with  $17''$  overlapping regions, limiting our sensitivity to objects with large angular diameters.



LSBG-750 has  $r_{\text{eff}} = 1.8$  kpc, making them similar in size and surface brightness to UDGs. However, they are distinct from most known UDGs in that they are star-forming, exist in the field, and were selected in the optical in an environmentally blind survey. In the case of LSBG-750, we set an upper limit on its rotational velocity of  $\lesssim 50 \text{ km s}^{-1}$ , which is comparable to dwarf galaxies of similar stellar mass with estimated halo masses of  $< 10^{11} M_{\odot}$  (Figure 5). We summarize the observed and inferred galaxy properties in Table 2.

We studied the stellar populations of these systems using UV–MIR matched-aperture photometry and the Bayesian SED fitting code *prospector*, assuming an exponentially declining star formation history for our fiducial model (see Figure 3 for the marginalized posterior distributions). The stellar populations of both objects are likely of intermediate age ( $\sim 1\text{--}3$  Gyr) and have undergone extended star formation histories characterized by low, but nonzero,  $e$ -folding time-scales ( $\tau < 1$  Gyr). Their current SFRs ( $\sim 0.002\text{--}0.01 M_{\odot} \text{ yr}^{-1}$ ) are low compared to gas-rich galaxies of similar stellar mass detected by ALFALFA, though they are consistent with the large scatter observed in the SFR–stellar mass relation for such objects. With stellar metallicities  $[Z_{\star}/Z_{\odot}] \lesssim -1.0$  and total stellar masses  $\sim 10^7 M_{\odot}$ , both galaxies are consistent with the observed stellar mass–metallicity relation for dwarf galaxies.

Based on our measurements of (or limits on) [O III]  $\lambda 5007$ , [N II]  $\lambda 6583$ , and  $\text{H}\alpha$  combined with the very low dust content in these galaxies (as evidenced by our SED fits), LSBG-285 and LSBG-750 fall on the star-forming locus of the BPT diagram, suggesting that we are observing emission from H II regions within these diffuse systems. Assuming the linear relation from Pettini & Pagel (2004) to convert [N II]  $\lambda 6583/\text{H}\alpha$  into oxygen abundance, our sources are consistent with having somewhat high gas-phase metallicity for their stellar mass (Figure 4). Higher signal-to-noise ratio observations and a better understanding of the true distribution of galaxies at such low surface brightnesses will be required to place these results in context with the better-studied, higher surface brightness galaxy population.

We thank the anonymous referee for their careful reading of our paper and their useful comments and suggestions. We thank Gonzalo Aniano for making his convolution kernels publicly available and for his assistance with generating additional *WISE* kernels. We thank Amy Reines for sharing her dwarf galaxy catalog. J.P.G. is grateful to Adrian Price-Whelan and Viraj Pandya for useful conversations. J.P.G. was supported by the National Science Foundation under grant No. AST 1713828.

The Hyper Suprime-Cam (HSC) Collaboration includes the astronomical communities of Japan and Taiwan, as well as Princeton University. The HSC instrumentation and software were developed by the National Astronomical Observatory of Japan (NAOJ), the Kavli Institute for the Physics and Mathematics of the Universe (Kavli IPMU), the University of Tokyo, the High Energy Accelerator Research Organization (KEK), the Academia Sinica Institute for Astronomy and Astrophysics in Taiwan (ASIAA), and Princeton University. Funding was contributed by the FIRST program from the Japanese Cabinet Office, the Ministry of Education, Culture, Sports, Science and Technology (MEXT), the Japan Society for the Promotion of Science (JSPS), Japan Science and

Technology Agency (JST), the Toray Science Foundation, NAOJ, Kavli IPMU, KEK, ASIAA, and Princeton University.

This paper makes use of software developed for the Large Synoptic Survey Telescope. We thank the LSST Project for making their code available as free software at <http://dm.lsst.org>.





Based in part on data collected at the Subaru Telescope and retrieved from the HSC data archive system, which is operated by the Subaru Telescope and Astronomy Data Center, National Astronomical Observatory of Japan.

The spectra presented in this work are based on observations obtained at the Gemini Observatory, which is operated by the Association of Universities for Research in Astronomy, Inc., under a cooperative agreement with the NSF on behalf of the Gemini partnership: the National Science Foundation (United States), the National Research Council (Canada), CONICYT (Chile), Ministerio de Ciencia, Tecnología e Innovación Productiva (Argentina), and Ministério da Ciência, Tecnologia e Inovação (Brazil).

This research has made use of the NASA/IPAC Extragalactic Database (NED), which is operated by the Jet Propulsion Laboratory, California Institute of Technology, under contract with the National Aeronautics and Space Administration.

*Software:* This work additionally utilized *astropy* (Astropy Collaboration et al. 2013), *numpy* (Van der Walt et al. 2011), *scipy* (<https://www.scipy.org>), *matplotlib* (Hunter 2007), *sfdmap* (<https://github.com/kbarbary/sfdmap>), and *corner* (Foreman-Mackey 2016).

## ORCID iDs

Johnny P. Greco  <https://orcid.org/0000-0003-4970-2874>  
Michael A. Strauss  <https://orcid.org/0000-0002-0106-7755>  
Song Huang  <https://orcid.org/0000-0003-1385-7591>  
Ji Hoon Kim  <https://orcid.org/0000-0002-1418-3309>

## References

- Aihara, H., Allende Prieto, C., An, D., et al. 2011, *ApJS*, **193**, 29
- Aihara, H., Arimoto, N., Armstrong, R., et al. 2018a, *PASJ*, **70**, S4
- Aihara, H., Armstrong, R., Bickerton, S., et al. 2018b, *PASJ*, **70**, S8
- Amorisco, N. C., & Loeb, A. 2016, *MNRAS*, **459**, L51
- Aniano, G., Draine, B. T., Gordon, K. D., & Sandstrom, K. 2011, *PASP*, **123**, 1218
- Astropy Collaboration, Robitaille, T. P., Tollerud, E. J., et al. 2013, *A&A*, **558**, A33
- Baldwin, J. A., Phillips, M. M., & Terlevich, R. 1981, *PASP*, **93**, 5
- Bellazzini, M., Belokurov, V., Magrini, L., et al. 2017, *MNRAS*, **467**, 3751
- Blanton, M. R., Lupton, R. H., Schlegel, D. J., et al. 2005, *ApJ*, **631**, 208
- Blanton, M. R., & Roweis, S. 2007, *AJ*, **133**, 734
- Bosch, J., Armstrong, R., Bickerton, S., et al. 2018, *PASJ*, **70**, S5
- Boylan-Kolchin, M., Bullock, J. S., & Kaplinghat, M. 2011, *MNRAS*, **415**, L40
- Bradford, J. D., Geha, M. C., & van den Bosch, F. C. 2016, *ApJ*, **832**, 11
- Bradley, L., Sipocz, B., Robitaille, T., et al. 2017, *astropy/photutils*: v0.4, Zenodo, doi:10.5281/zenodo.1039309
- Bullock, J. S., & Boylan-Kolchin, M. 2017, *ARA&A*, **55**, 343
- Calzetti, D., Armus, L., Bohlin, R. C., et al. 2000, *ApJ*, **533**, 682
- Cannon, J. M., Giovanelli, R., Haynes, M. P., et al. 2011, *ApJL*, **739**, L22
- Cardelli, J. A., Clayton, G. C., & Mathis, J. S. 1989, *ApJ*, **345**, 245
- Chabrier, G. 2003, *PASP*, **115**, 763
- Chan, T. K., Kereš, D., Wetzel, A., et al. 2018, *MNRAS*, **478**, 906
- Collins, M. L. M., Chapman, S. C., Rich, R. M., et al. 2013, *ApJ*, **768**, 172
- Conroy, C., Gunn, J. E., & White, M. 2009, *ApJ*, **699**, 486
- Conselice, C. J., Gallagher, J. S., III, & Wyse, R. F. G. 2003, *AJ*, **125**, 66
- Dalcanton, J. J., Spergel, D. N., Gunn, J. E., Schmidt, M., & Schneider, D. P. 1997, *AJ*, **114**, 635
- Danieli, S., van Dokkum, P., & Conroy, C. 2018, *ApJ*, **856**, 69

- de Blok, W. J. G., & Bosma, A. 2002, *A&A*, **385**, 816
- de Blok, W. J. G., McGaugh, S. S., Bosma, A., & Rubin, V. C. 2001, *ApJL*, **552**, L23
- Dekel, A., & Silk, J. 1986, *ApJ*, **303**, 39
- Di Cintio, A., Brook, C. B., Dutton, A. A., et al. 2017, *MNRAS*, **466**, L1
- Disney, M. J. 1976, *Natur*, **263**, 573
- El-Badry, K., Wetzel, A., Geha, M., et al. 2016, *ApJ*, **820**, 131
- Ellison, S. L., Patton, D. R., Simard, L., & McConnachie, A. W. 2008, *ApJL*, **672**, L107
- Falcón-Barroso, J., Sánchez-Blázquez, P., Vazdekis, A., et al. 2011, *A&A*, **532**, A95
- Ferre-Mateu, A., Alabi, A., Forbes, D. A., et al. 2018, *MNRAS*, **479**, 4891
- Foreman-Mackey, D. 2016, *JOSS*, **1**, 24
- Foreman-Mackey, D., Hogg, D. W., Lang, D., & Goodman, J. 2013, *PASP*, **125**, 306
- Furusawa, H., Koike, M., Takata, T., et al. 2018, *PASJ*, **70**, S3
- Geha, M., Blanton, M. R., Yan, R., & Tinker, J. L. 2012, *ApJ*, **757**, 85
- Giovanelli, R., Haynes, M. P., Adams, E. A. K., et al. 2013, *AJ*, **146**, 15
- Giovanelli, R., Haynes, M. P., Kent, B. R., et al. 2005, *AJ*, **130**, 2598
- Governato, F., Brook, C., Mayer, L., et al. 2010, *Natur*, **463**, 203
- Greco, J. P., Greene, J. E., Strauss, M. A., et al. 2018, *ApJ*, **857**, 104
- Gu, M., Conroy, C., Law, D., et al. 2018, *ApJ*, **859**, 37
- Haurberg, N. C., Salzer, J. J., Cannon, J. M., & Marshall, M. V. 2015, *ApJ*, **800**, 121
- Holmberg, E. 1958, *MeLuS*, **136**, 1
- Huang, S., Haynes, M. P., Giovanelli, R., & Brinchmann, J. 2012, *ApJ*, **756**, 113
- Hunter, D. A., Ficut-Vicas, D., Ashley, T., et al. 2012, *AJ*, **144**, 134
- Hunter, D. A. 2007, *CSE*, **9**, 90
- Jester, S., Schneider, D. P., Richards, G. T., et al. 2005, *AJ*, **130**, 873
- Johnson, B., & Leja, J. 2017, bd-j/prospector: Initial release, Zenodo, doi:10.5281/zenodo.1116491
- Kadowaki, J., Zaritsky, D., & Donnerstein, R. L. 2017, *ApJL*, **838**, L21
- Karachentsev, I. D., Makarov, D. I., & Kaisina, E. I. 2013, *AJ*, **145**, 101
- Karachentsev, I. D., Makarova, L. N., Sharina, M. E., & Karachentseva, V. E. 2017, *AstBu*, **72**, 376
- Kauffmann, G., Heckman, T. M., Tremonti, C., et al. 2003, *MNRAS*, **346**, 1055
- Kennicutt, R. C., Jr. 1998, *ARA&A*, **36**, 189
- Kirby, E. N., Cohen, J. G., Guhathakurta, P., et al. 2013, *ApJ*, **779**, 102
- Koda, J., Yagi, M., Yamanoi, H., & Komiyama, Y. 2015, *ApJL*, **807**, L2
- Komiyama, Y., Obuchi, Y., Nakaya, H., et al. 2018, *PASJ*, **70**, S2
- Lang, D. 2014, *AJ*, **147**, 108
- Larson, R. B. 1974, *MNRAS*, **169**, 229
- Lee, J. C., Gil de Paz, A., Tremonti, C., et al. 2009, *ApJ*, **706**, 599
- Leisman, L., Haynes, M. P., Janowiecki, S., et al. 2017, *ApJ*, **842**, 133
- Leja, J., Johnson, B. D., Conroy, C., van Dokkum, P. G., & Byler, N. 2017, *ApJ*, **837**, 170
- Lupton, R., Blanton, M. R., Fekete, G., et al. 2004, *PASP*, **116**, 133
- Marchesini, D., D’Onghia, E., Chincarini, G., et al. 2002, *ApJ*, **575**, 801
- Marigo, P., & Girardi, L. 2007, *A&A*, **469**, 239
- Marigo, P., Girardi, L., Bressan, A., et al. 2008, *A&A*, **482**, 883
- Martin, D. C., Fanson, J., Schiminovich, D., et al. 2005, *ApJL*, **619**, L1
- Martínez-Delgado, D., Läsker, R., Sharina, M., et al. 2016, *AJ*, **151**, 96
- McConnachie, A. W. 2012, *AJ*, **144**, 4
- Meisner, A. M., Lang, D., & Schlegel, D. J. 2017a, *AJ*, **153**, 38
- Meisner, A. M., Lang, D., & Schlegel, D. J. 2017b, *AJ*, **154**, 161
- Miyazaki, S., Komiyama, Y., Kawanomoto, S., et al. 2018, *PASJ*, **70**, S1
- Mould, J. R., Huchra, J. P., Freedman, W. L., et al. 2000, *ApJ*, **529**, 786
- Moustakas, J., Kennicutt, R. C., Jr., & Tremonti, C. A. 2006, *ApJ*, **642**, 775
- Oh, S.-H., Hunter, D. A., Brinks, E., et al. 2015, *AJ*, **149**, 180
- Oke, J. B., & Gunn, J. E. 1983, *ApJ*, **266**, 713
- Osterbrock, D. E. 1989, *Astrophysics of Gaseous Nebulae and Active Galactic Nuclei* (Mill Valley, CA: Univ. Sci. Books)
- Pandya, V., Romanowsky, A. J., Laine, S., et al. 2018, *ApJ*, **858**, 29
- Papastergis, E., Adams, E. A. K., & Romanowsky, A. J. 2017, *A&A*, **601**, L10
- Papastergis, E., Giovanelli, R., Haynes, M. P., & Shankar, F. 2015, *A&A*, **574**, A113
- Pettini, M., & Pagel, B. E. J. 2004, *MNRAS*, **348**, L59
- Reines, A. E., Greene, J. E., & Geha, M. 2013, *ApJ*, **775**, 116
- Román, J., & Trujillo, I. 2017a, *MNRAS*, **468**, 703
- Román, J., & Trujillo, I. 2017b, *MNRAS*, **468**, 4039
- Ruiz-Lara, T., Beasley, M. A., Falcón-Barroso, J., et al. 2018, *MNRAS*, **478**, 2034
- Sánchez Almeida, J., & Dalla Vecchia, C. 2018, *ApJ*, **859**, 109
- Sánchez-Blázquez, P., Peletier, R. F., Jiménez-Vicente, J., et al. 2006, *MNRAS*, **371**, 703
- Sandage, A., & Binggeli, B. 1984, *AJ*, **89**, 919
- Sanders, R. L., Shapley, A. E., Zhang, K., & Yan, R. 2017, *ApJ*, **850**, 136
- Schlaflly, E. F., & Finkbeiner, D. P. 2011, *ApJ*, **737**, 103
- Schlegel, D. J., Finkbeiner, D. P., & Davis, M. 1998, *ApJ*, **500**, 525
- Spekkens, K., & Karunakaran, A. 2018, *ApJ*, **855**, 28
- Tollerud, E. J., Geha, M. C., Grcevich, J., Putman, M. E., & Stern, D. 2015, *ApJL*, **798**, L21
- Torres-Flores, S., Epinat, B., Amram, P., Plana, H., & Mendes de Oliveira, C. 2011, *MNRAS*, **416**, 1936
- Trujillo, I., Roman, J., Filho, M., & Sánchez Almeida, J. 2017, *ApJ*, **836**, 191
- van der Burg, R. F. J., Hoekstra, H., Muzzin, A., et al. 2017, *A&A*, **607**, A79
- van der Burg, R. F. J., Muzzin, A., & Hoekstra, H. 2016, *A&A*, **590**, A20
- Van der Walt, S., Colbert, S. C., & Varoquaux, G. 2011, *CSE*, **13**, 22
- van Dokkum, P., Abraham, R., Brodie, J., et al. 2016, *ApJL*, **828**, L6
- van Dokkum, P. G., Abraham, R., Merritt, A., et al. 2015, *ApJL*, **798**, L45
- Weinberg, D. H., Bullock, J. S., Governato, F., Kuzio de Naray, R., & Peter, A. H. G. 2015, *PNAS*, **112**, 12249
- Wright, E. L., Eisenhardt, P. R. M., Mainzer, A. K., et al. 2010, *AJ*, **140**, 1868
- Wyder, T. K., Martin, D. C., Schiminovich, D., et al. 2007, *ApJS*, **173**, 293
- Yagi, M., Koda, J., Komiyama, Y., & Yamanoi, H. 2016, *ApJS*, **225**, 11
- Yozin, C., & Bekki, K. 2015, *MNRAS*, **452**, 937